

UC Santa Barbara

UC Santa Barbara Previously Published Works

Title

A settling-driven instability in two-component, stably stratified fluids

Permalink

<https://escholarship.org/uc/item/6fn5t93z>

Authors

Alsinan, A
Meiburg, E
Garaud, P

Publication Date

2017-04-10

DOI

10.1017/jfm.2017.94

Peer reviewed

A settling-driven instability in two-component, stably stratified fluids

A. Alsinan¹, E. Meiburg^{1,†} and P. Garaud²

¹Department of Mechanical Engineering, University of California at Santa Barbara, Santa Barbara, CA 93106, USA

²Department of Applied Mathematics and Statistics, Baskin School of Engineering, University of California at Santa Cruz, Santa Cruz, CA 95064, USA

(Received 13 October 2016; revised 6 February 2017; accepted 7 February 2017)

We analyse the linear stability of stably stratified fluids whose density depends on two scalar fields where one of the scalar fields is unstably stratified and involves a settling velocity. Such conditions may be found, for example, in flows involving the transport of sediment in addition to heat or salt. A linear stability analysis for constant-gradient base states demonstrates that the settling velocity generates a phase shift between the perturbation fields of the two scalars, which gives rise to a novel, settling-driven instability mode. This instability mechanism favours the growth of waves that are inclined with respect to the horizontal. It is active for all density and diffusivity ratios, including for cases in which the two scalars diffuse at identical rates. If the scalars have unequal diffusivities, it competes with the elevator mode waves of the classical double-diffusive instability. We present detailed linear stability results as a function of the governing dimensionless parameters, including for lateral gradients of the base state density fields that result in predominantly horizontal intrusion instabilities. Highly resolved direct numerical simulation results serve to illustrate the nonlinear competition of the various instabilities for such flows in different parameter regimes.

Key words: double diffusive convection, sediment transport, stratified flows

1. Introduction

Stably stratified fluids whose density is a function of two scalar fields can give rise to double-diffusive instabilities, provided these two scalars diffuse at different rates and one of them is unstably stratified. An important example concerns the world's oceans, as heat diffuses approximately one hundred times more rapidly than salt. When warm, salty water overlies cooler, fresher water, so that the more slowly diffusing scalar is unstably stratified, we commonly observe an exponentially growing instability called salt fingering. By contrast, if the cold and fresh water is on top, the evolving instability in the form of diffusive convection is oscillatory in nature. In both cases, the resulting instability can contribute significantly to vertical transport. Other environments in which double-diffusion plays an important role include magmas, metals and stellar interiors (Turner 1985). The first rigorous quantitative analysis

† Email address for correspondence: meiburg@engineering.ucsb.edu

of double-diffusive instabilities was provided by Stern (1960), and a comprehensive review of the field is given in the beautiful, recent book by Radko (2013).

In the present work, we aim to understand how the traditional picture of double diffusion is modified if the unstably stratified scalar is a particulate phase with a Stokes settling velocity. A number of laboratory flow visualization experiments (Green 1987; Green & Diez 1995; Carey 1997; Chen 1997; Hoyal, Bursik & Atkinson 1999*a,b*; Maxworthy 1999; Parsons & García 2000; Parsons, Bush & Syvitski 2001; Manville & Wilson 2004; Carazzo & Jellinek 2013; Manzella *et al.* 2015; Rouhnia & Strom 2015; Davarpanah & Wells 2016) demonstrate that thermal or compositional density gradients can dramatically alter the effective settling velocity of the particles by driving double-diffusive instabilities or settling-driven convection. This mechanism has also been hypothesized to be active in the field observations by Scheu *et al.* (2015), and in the lake measurements of Sánchez & Roget (2007). Nevertheless, a detailed quantitative understanding of double-diffusive instabilities involving a sediment phase has not yet been achieved, and predictive scaling laws for vertical transport remain largely absent. Progress in this direction will contribute to our insight into a wide range of processes, among them the outflow of sediment from buoyant river plumes into colder lakes or the saline ocean, the dynamics of certain classes of clouds, as well as ecological, astrophysical and engineering applications.

Some first insight into the ways in which the presence of a settling velocity can modify the stability of two-component systems is provided by the linear stability analyses of Burns & Meiburg (2012) and Yu, Hsu & Balachandar (2013), as well as by the nonlinear simulations of Yu, Hsu & Balachandar (2014) and Burns & Meiburg (2015). Those authors address the configuration of fresh, sediment-laden water above salty, clear water, with piecewise constant profiles of salinity and sediment concentration. Under such conditions, particle settling will result in the formation of an interfacial ‘nose region’ that contains both sediment and salinity. On the lower side of this nose region, Rayleigh–Taylor instabilities can emerge that compete with double-diffusive instabilities, as analysed in detail by the direct numerical simulations (DNS) of Burns & Meiburg (2015). These simulations indicate that the effective, double-diffusive settling velocity of sediment under such conditions can be more than an order of magnitude larger than the Stokes settling velocity. The opposite case of clear, salty water above fresh, sediment-laden water is addressed by Schulte, Konopliv & Meiburg (2016). In the present investigation, on the other hand, we will focus on constant-gradient base states for both sediment and salinity concentration, so that a nose region and corresponding Rayleigh–Taylor instability will not form. Instead, as will be seen in the following, we observe the emergence of a novel instability mode driven entirely by the settling velocity. The competition between this settling-driven mode and traditional double-diffusive instability modes determines the dynamical evolution of the flow.

The physical mechanisms to be investigated here are not limited to oceanic sediment transport, however. They are also active in the transport of nutrients and possibly phytoplankton in estuaries and the coastal oceans, with wide-ranging ecological implications, and they may be important for the downward flux of biogenic ‘marine snow’, which forms the basis of deep-sea ecosystems (Alldredge & Cohen 1987). Marine snow represents the main vehicle by which CO₂ is transported from the surface layers towards the deep ocean. Understanding the dynamics of this transport process is essential for predicting the uptake rate of atmospheric CO₂ by the world’s oceans – a quantity of fundamental importance in all global climate models. Because of the long residence time of the ocean’s thermohaline circulation,

carbon transported as marine snow into the deep ocean can remain out of contact with the atmosphere for >1000 years. Hence, when the marine snow is finally decomposed to inorganic nutrients and dissolved carbon dioxide, these are effectively isolated from the surface ocean for the relatively long time scales associated with ocean circulation. Consequently, enhancing the quantity of marine snow that reaches the deep ocean forms the basis of geoengineering schemes intended to enhance carbon sequestration by the ocean. These schemes propose the iron fertilization of the surface ocean in order to boost the production of organic material, with a concomitant rise in marine snow reaching the deep ocean (Lampitt *et al.* 2008).

This paper is structured as follows: § 2 defines the physical problem and formulates the governing equations in the Boussinesq limit for a generic two-component ‘heat/sediment system’ in which the unstably stratified sediment concentration field has a net settling velocity. By non-dimensionalizing these equations, we identify five governing dimensionless parameters in the form of a Prandtl number, a density ratio, a diffusivity ratio, a non-dimensional settling velocity and the ratio of the lateral gradients of the base state density profiles. Section 3 carries out the linear stability analysis and derives a cubic polynomial for the complex growth rate of unstable modes as a function of the horizontal and vertical wavenumbers and the dimensionless parameters. Section 4 discusses solutions to this polynomial, with an emphasis on the role of the settling velocity. We observe the novel instability mode alluded to above that results from the presence of the settling velocity, which destabilizes waves that are inclined with respect to the horizontal direction. In the presence of double diffusion these unstable inclined waves overtake the classical ‘elevator modes’ beyond a critical value of the settling velocity. A detailed analysis of the eigenfunctions identifies the key physical mechanism responsible for the destabilization of inclined waves in terms of a phase shift between the temperature and sediment perturbations, and hence between the stabilizing and destabilizing vorticity components generated by these two scalars. The new, settling-driven instability mode exists entirely separately from the double-diffusive mode, and causes the flow to be unstable even if both scalars diffuse at the same rate. The presence of lateral gradients breaks the symmetry of the problem, and in the classical heat/salt system it results in the appearance of an intrusive instability mode, with intrusions propagating predominantly in the lateral direction, but at an angle to the horizontal (Stern 1967; Ruddick & Turner 1979; Holyer 1983; Medrano, Garaud & Stellmach 2014). Here we will analyse the competition between this intrusive mode and the new, settling-driven mode. Section 5 discusses representative direct numerical simulation results that illustrate the nonlinear evolution of the flow in different parameter regimes. These simulations demonstrate the evolution of traditional, double-diffusive fingering and intrusion instabilities, as well as settling-driven inclined waves and secondary instabilities in the form of horizontal layers. The mechanisms for the formation of these horizontal layers is analysed in detail in the companion paper by Reali *et al.* (2017). Section 6 presents a brief summary of our findings.

2. Problem formulation

We consider an unbounded domain of fluid initially at rest, as shown in figure 1. This fluid contains a rapidly diffusing scalar, ‘heat’, and the more slowly diffusing ‘sediment’, both of which affect its density in a linear fashion. In the base state, the temperature $T(x, z)$ and sediment concentration $C(x, z)$ depend linearly on the vertical and horizontal coordinates, z and x . While the overall density profile is stably stratified,

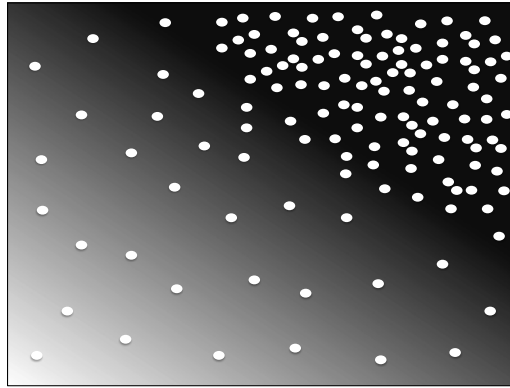


FIGURE 1. Schematic of the base state: we consider an overall stably stratified fluid whose density depends on two components. One of them ('heat') is stably stratified, while the second one ('sediment') is unstably stratified and settles with a constant velocity. The horizontal temperature and sediment concentration gradients are density compensating, so that the base state density profile depends only on the vertical coordinate. Darker shading indicates higher temperature, while the white dots represent sediment grains.

the sediment concentration field by itself is unstably stratified. The horizontal gradients are assumed to be density compensating, so that the overall density of the base state is independent of the horizontal direction.

2.1. Governing equations

We analyse the flow based on the two-dimensional Navier–Stokes equations for incompressible flow

$$\nabla \cdot \mathbf{u} = 0, \tag{2.1}$$

$$\rho \left(\frac{\partial \mathbf{u}}{\partial t} + \mathbf{u} \cdot \nabla \mathbf{u} \right) = \mu \nabla^2 \mathbf{u} - \nabla p + (\rho - \rho_m) \mathbf{g}, \tag{2.2}$$

where $\mathbf{u} = (u, w)$ indicates the fluid velocity vector, \mathbf{g} represents the acceleration due to gravity in the $-z$ -direction, μ denotes the dynamic viscosity, p is the pressure and ρ_m indicates a reference density value. The fluid density ρ depends on the temperature and sediment concentration as

$$\rho = \rho_m (1 - \alpha(T - T_m) + \beta(C - C_m)), \tag{2.3}$$

where (T_m, C_m) represent reference values for temperature and concentration and the coefficients (α, β) reflect the dependence of the density on the temperature and sediment concentration, respectively. Since the density differences in a typical ocean environment are small, we apply the Boussinesq approximation. This allows us to neglect density variations everywhere except in the buoyancy term that drives the fluid motion, so that we can replace ρ on the left-hand side of (2.2) with ρ_m .

The temperature and sediment concentration fields are governed by the convection–diffusion transport equations

$$\frac{\partial T}{\partial t} + \mathbf{u} \cdot \nabla T = \kappa_T \nabla^2 T, \tag{2.4}$$

$$\frac{\partial C}{\partial t} + \mathbf{u} \cdot \nabla C - W_{st}^* \frac{\partial C}{\partial z} = \kappa_c \nabla^2 C, \tag{2.5}$$

where κ_T and κ_C indicate the thermal and sediment diffusivities, respectively, which are assumed to have constant values, with $\kappa_T > \kappa_C$. W_{st}^* represents the constant Stokes settling velocity of the monodisperse sediment.

We will investigate the linear stability of a base state in which the fluid is assumed to be at rest. The temperature and sediment concentration fields of the base state, $T_0(x, z)$ and $C_0(x, z, t)$, depend linearly on the horizontal and vertical directions

$$T_0(x, z) = T_{0x}x + T_{0z}z, \tag{2.6}$$

$$C_0(x, z, t) = C_{0x}x + C_{0z}(z + W_{st}^*t), \tag{2.7}$$

where T_{0x} , T_{0z} , C_{0x} and C_{0z} are constants. Since the horizontal temperature and sediment concentration gradients are assumed to be density compensating, we have $\alpha T_{0x} = \beta C_{0x}$. Note that C_0 cannot be constant in time, but must instead have a linear time dependence to account for settling. However, the base state concentration gradients are constant with time.

2.2. Characteristic scales

To non-dimensionalize the governing equations, we adopt the standard characteristic scales of double-diffusive flow as reviewed by Radko (2013). As length scale, we choose the expected finger width

$$[d] = \left(\frac{\kappa_T \nu}{g \alpha T_{0z}} \right)^{1/4}, \tag{2.8}$$

where $\nu = \mu / \rho_m$ denotes the kinematic viscosity and T_{0z} represents the magnitude of the base state vertical temperature gradient. Typical values in the mid-latitude thermocline are $T_{0z} \sim 0.01 \text{ }^\circ\text{C m}^{-1}$ and $d \sim 0.01 \text{ m}$ (Radko 2013). As characteristic scales for time, velocity, temperature and sediment concentration, respectively, we obtain

$$[t] = \frac{d^2}{\kappa_T}, \tag{2.9}$$

$$[u] = \frac{\kappa_T}{d}, \tag{2.10}$$

$$[T] = T_{0z}d, \tag{2.11}$$

$$[C] = \frac{\alpha}{\beta} T_{0z}d. \tag{2.12}$$

In this way, we arrive at the following set of governing dimensionless equations for the heat–sediment system

$$\frac{1}{Pr} \left(\frac{\partial \mathbf{u}}{\partial t} + \mathbf{u} \cdot \nabla \mathbf{u} \right) = \nabla^2 \mathbf{u} - \nabla p + (T - C) \hat{\mathbf{k}}, \tag{2.13}$$

$$\frac{\partial T}{\partial t} + \mathbf{u} \cdot \nabla T = \nabla^2 T, \tag{2.14}$$

$$\frac{\partial C}{\partial t} + \mathbf{u} \cdot \nabla C - W_{st} \frac{\partial C}{\partial z} = \tau \nabla^2 C, \tag{2.15}$$

$$\nabla \cdot \mathbf{u} = 0, \tag{2.16}$$

where all quantities have now been non-dimensionalized. The dimensionless parameters in the form of the Prandtl number Pr , a diffusivity ratio τ and a settling velocity W_{st} are defined as

$$Pr = \frac{\nu}{\kappa_T}, \quad \tau = \frac{\kappa_C}{\kappa_T}, \quad W_{st} = \frac{W_{st}^* d}{\kappa_T}. \tag{2.17a-c}$$

A further dimensionless quantity arises via the base state in the form of the so-called density ratio R_ρ

$$R_\rho = \frac{\alpha T_{0z}}{\beta C_{0z}}, \tag{2.18}$$

which measures the relative strength of the stabilizing vertical temperature gradient and the destabilizing vertical sediment gradient of the base state (Turner 1979).

3. Linear stability analysis

The base state is defined by fluid at rest, along with the dimensionless temperature and sediment concentration fields

$$T_0(x, z) = \phi x + z, \tag{3.1}$$

$$C_0(x, z, t) = \phi x + \frac{1}{R_\rho} (z + W_{st} t). \tag{3.2}$$

Here, ϕ is the slope of lines of constant $T_0(x, z)$, defined as

$$\phi = \frac{T_{0x}}{T_{0z}}, \tag{3.3}$$

where T_{0x} and T_{0z} are dimensional values.

In order to conduct a linear stability analysis, we decompose the dimensionless velocity, temperature and sediment fields into their base states and perturbations

$$u(x, z, t) = u'(x, z, t), \tag{3.4}$$

$$w(x, z, t) = w'(x, z, t), \tag{3.5}$$

$$T(x, z, t) = T_0(x, z) + T'(x, z, t), \tag{3.6}$$

$$C(x, z, t) = C_0(x, z, t) + C'(x, z, t), \tag{3.7}$$

where u' , T' and C' denote perturbations away from the base state. We assume these perturbations to be small, so that (2.13)–(2.16) can be linearized by neglecting terms that are quadratic in the perturbations. After dropping the primes, we obtain

$$\frac{1}{Pr} \frac{\partial u}{\partial t} + \frac{\partial p}{\partial x} - \nabla^2 u = 0, \tag{3.8}$$

$$\frac{1}{Pr} \frac{\partial w}{\partial t} + \frac{\partial p}{\partial z} - \nabla^2 w + (C - T) = 0, \tag{3.9}$$

$$\frac{\partial T}{\partial t} + \phi u + w - \nabla^2 T = 0, \tag{3.10}$$

$$\frac{\partial C}{\partial t} + \phi u + \frac{1}{R_\rho} w - W_{st} \frac{\partial C}{\partial z} - \tau \nabla^2 C = 0, \tag{3.11}$$

$$\frac{\partial u}{\partial x} + \frac{\partial w}{\partial z} = 0. \tag{3.12}$$

The linear stability problem is thus fully defined by the dimensionless parameters Pr , τ , W_{st} , ϕ and R_ρ .

We now eliminate the pressure terms by cross-differentiating the momentum equation components, thus obtaining

$$\left(\frac{1}{Pr} \frac{\partial}{\partial t} - \nabla^2 \right) \left(\frac{\partial u}{\partial z} - \frac{\partial w}{\partial x} \right) + \frac{\partial T}{\partial x} - \frac{\partial C}{\partial x} = 0. \tag{3.13}$$

This equation describes the generation of vorticity $\omega = (\partial w / \partial x) - (\partial u / \partial z)$ as a result of horizontal temperature and sediment concentration gradients.

We examine the stability of the system using normal modes of the form

$$(u, w, T, C) \sim \text{Re}[(\hat{u}, \hat{w}, \hat{T}, \hat{C}) \exp(\lambda t + i l x + i k z)], \tag{3.14}$$

where $\lambda = \lambda_R + i \lambda_I$ represents the complex growth rate. The quantities l and k denote the real horizontal and vertical wavenumbers, respectively, while \hat{u} , \hat{w} , \hat{T} and \hat{C} indicate the amplitudes of the respective Fourier modes. Substitution into the continuity (3.12) gives

$$\hat{u} = -\frac{k}{l} \hat{w}. \tag{3.15}$$

By substituting the normal modes into (3.13), we obtain

$$\left(\frac{\lambda}{Pr} + K^2 \right) (i k \hat{u} - i l \hat{w}) + i l (\hat{T} - \hat{C}) = 0, \tag{3.16}$$

where $K^2 = l^2 + k^2$. Further straightforward algebraic manipulations yield the final form of the system as

$$\left(\frac{\lambda}{Pr} + K^2 \right) \left(\frac{K^2}{l^2} \right) \hat{w} = (\hat{T} - \hat{C}), \tag{3.17}$$

$$(\lambda + K^2) \hat{T} = \left(\frac{\phi k}{l} - 1 \right) \hat{w}, \tag{3.18}$$

$$(\lambda + \tau K^2 - W_{st} i k) \hat{C} = \left(\frac{\phi k}{l} - \frac{1}{R_\rho} \right) \hat{w}. \tag{3.19}$$

These equations can be combined into a single cubic expression for the complex growth rate

$$\lambda^3 + a_2 \lambda^2 + a_1 \lambda + a_0 = 0, \tag{3.20}$$

where

$$a_2 = K^2 (1 + Pr + \tau) - i W_{st} k, \tag{3.21}$$

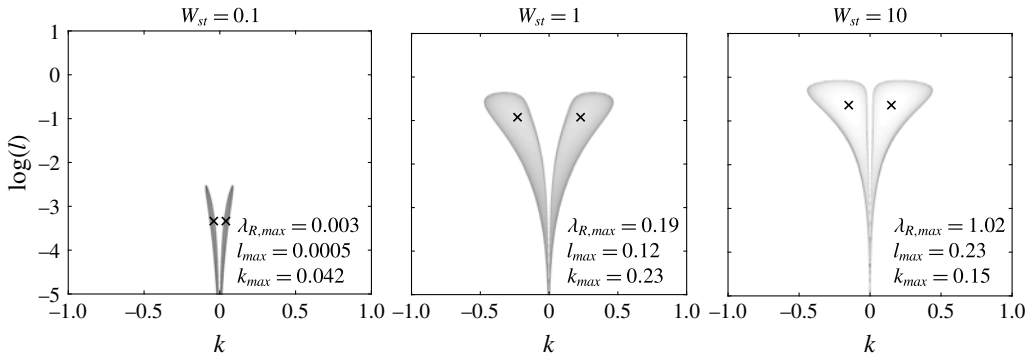


FIGURE 2. $Pr = 7$, $\tau = 1$, $R_\rho = 1.5$, $\phi = 0$: maximum real part λ_R of the growth rate as function of the vertical (k) and horizontal (l) wavenumbers, for three different values of the particle settling velocity W_{st} . Only positive values of λ_R are shown, and the mode with the largest growth rate $\lambda_{R,max}$ is marked with an ‘x’. The grey shading is scaled to $\log(\lambda_R)$. Since the two scalars have equal diffusivities ($\tau = 1$), the system is stable with regard to double diffusion, and the instability is driven purely by settling. The dominant mode has the shape of inclined waves, and both the maximum growth rate $\lambda_{R,max}$ and the unstable wavenumber range increase with W_{st} .

$$a_1 = K^4(\tau + Pr + \tau Pr) + Pr \frac{l^2}{K^2} \left(1 - \frac{1}{R_\rho}\right) - iK^2 W_{st} k(1 + Pr), \tag{3.22}$$

$$a_0 = \tau Pr K^6 + Pr l^2 \left(\tau - \frac{1}{R_\rho}\right) + Pr l k \phi(1 - \tau) + \frac{iPr W_{st} k}{K^2} (\phi l k - l^2 - K^6). \tag{3.23}$$

In contrast to the traditional thermohaline double-diffusive system, the coefficients in the above cubic equation for the heat–sediment system are complex, as a result of the settling velocity term in the governing equations. When $W_{st} = 0$, our cubic system reduces to the one obtained by Holyer (1983). When $\phi = 0$, we recover the results of Reali *et al.* (2017).

In the following, we will analyse solutions of the above system, in terms of both growth rates and eigenfunctions.

4. Results

4.1. Settling-driven instability

4.1.1. Growth rate

In order to clarify the role of settling, we begin by discussing the idealized case without double-diffusive instabilities ($\tau = 1$), which is well known to be stable in the absence of settling. Figure 2 demonstrates that non-zero settling velocities drive instabilities, in spite of the overall stable density stratification. To the best of our knowledge, this purely settling-driven instability has not been reported before. The figure displays the maximum value of the real part of the growth rate, λ_R , as a function of the horizontal and vertical wavenumbers l and k , for three different values of the settling velocity W_{st} . The other parameter values are held fixed at $Pr = 7$, $\tau = 1$, $R_\rho = 1.5$ and $\phi = 0$, so that there are no lateral base state gradients. We observe the existence of two symmetric, lobe-shaped unstable regions for $k > 0$ and $k < 0$, while the ‘elevator’ mode $k = 0$ is always stable. The maximum growth rate $\lambda_{R,max}$ is seen to increase with W_{st} .

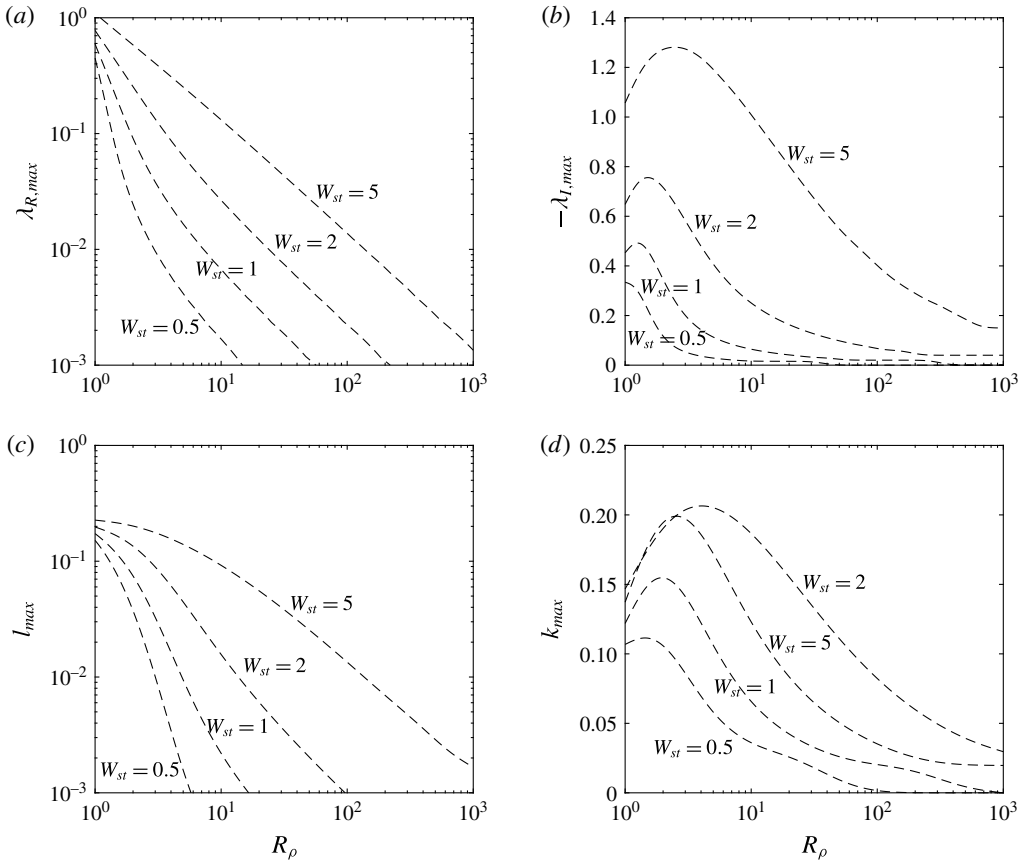


FIGURE 3. $Pr = 7$, $\tau = 1$, $\phi = 0$: dependence of the dominant mode properties on the density ratio R_ρ , for selected values of the settling velocity W_{st} . Since double diffusion is absent, the instability is driven purely by settling, and the case $W_{st} = 0$ is stable. (a) The maximum growth rate $\lambda_{R,max}$ increases uniformly with W_{st} , and decreases monotonically for larger values of R_ρ . (b) The imaginary part $\lambda_{I,max}$ of the growth rate of the dominant mode. This mode has the form of a downward travelling inclined wave. (c) The horizontal wavenumber l_{max} of the dominant mode increases with W_{st} but decreases with R_ρ . (d) The vertical wavenumber k_{max} of the dominant mode increases with W_{st} , and peaks for intermediate density ratios.

Figure 3 demonstrates that this settling-driven instability can be present for all values of the density ratio R_ρ , although the growth rate decreases with increasing R_ρ . The horizontal wavelength of the dominant mode grows monotonically with R_ρ and decreases for larger W_{st} , while its vertical wavenumber is seen to peak at intermediate values of R_ρ .

4.1.2. Eigenfunctions

Key to understanding the mechanism driving this new instability is (3.13), which states that vorticity is produced as a result of horizontal gradients in the temperature and sediment concentration fields. Equation (3.13) allows us to develop a vorticity-based physical interpretation of the linear stability behaviour in the presence

of horizontal temperature and sediment concentration perturbations. Since the base state temperature profile is stably stratified, the vorticity generated as a result of $\partial T/\partial x$ (the ‘ T -vorticity’) is of such a sign that it wants to return the flow to the base state. Hence we refer to the T -vorticity as being stabilizing. This is in contrast to any vorticity generated by $\partial C/\partial x$ (the ‘ C -vorticity’), which wants to move the flow further away from the base state and hence is destabilizing. Comparing the strength of the stabilizing T -vorticity to the destabilizing C -vorticity will hence allow us to gain insight into the overall stability of the flow. As a consequence of the characteristic temperature and concentration scales introduced above, static stability of the base profile implies $R_\rho > 1$. Hence, in the absence of diffusion and settling, any convective distortion of the base profile will result in $|\partial T/\partial x| > |\partial C/\partial x|$ everywhere. Consequently, equation (3.13) states that the stabilizing T -vorticity always outweighs the destabilizing C -vorticity at the same location, so that the overall system is stable. In the present context, there exist two potential scenarios for modifying the balance between the stabilizing T -vorticity and the destabilizing C -vorticity. First, double diffusion can render the flow unstable by smoothing out $\partial T/\partial x$ -gradients more rapidly than $\partial C/\partial x$ -gradients, so that the destabilizing C -vorticity outweighs the stabilizing T -vorticity in the same location. In addition there is the second possibility that the presence of a settling velocity for the sediment concentration field can shift the corresponding T - and C -contours relative to each other, so that the stabilizing T -vorticity may no longer be able to overcome the destabilizing C -vorticity everywhere, which again can render the overall system unstable. Both of these scenarios are discussed below.

In order to understand why the presence of the settling velocity destabilizes inclined waves $k \neq 0$, but not the elevator mode $k = 0$, we examine the eigenfunctions of the velocity components, vorticity, temperature and sediment concentration

$$\begin{pmatrix} w \\ u \\ \omega \\ T \\ C \end{pmatrix} = \text{Re} \left[\begin{pmatrix} \hat{w} \\ -\frac{k}{l}\hat{w} \\ \frac{(l^2 + k^2)i}{l}\hat{w} \\ \hat{T} \\ \hat{C} \end{pmatrix} e^{ilx+ikz} \right] \tag{4.1}$$

in light of this vorticity-based physical interpretation. For $k = 0$, the temperature and sediment perturbations do not depend on the vertical z -coordinate, so that they are not modified by vertical advection due to settling. Hence the elevator mode, which is stable for $\tau = 1$ in the absence of settling, remains stable when a settling velocity is present. For modes with $k \neq 0$, on the other hand, a different picture emerges, cf. figure 4. Compared to the inclined temperature contours, the contours of the sediment concentration field are now shifted downward by the settling velocity, so that at a constant z -location a horizontal phase shift emerges between the temperature and sediment concentration contours, and hence between the stabilizing T - and the destabilizing C -vorticity. Consequently, the stabilizing T -vorticity can no longer overcome the destabilizing C -vorticity everywhere, so that inclined modes with $k \neq 0$ are destabilized. This picture is confirmed by figure 5, which shows the two-dimensional unstable eigenmodes for temperature, sediment concentration and vorticity, together with the superimposed velocity vectors.

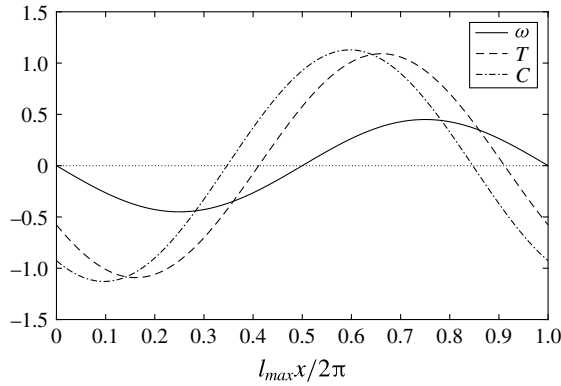


FIGURE 4. $Pr = 7$, $\tau = 1$, $R_\rho = 1.5$, $\phi = 0$, $W_{st} = 2$: horizontal cross-cut of the normalized two-dimensional dominant mode eigenfunctions for vorticity ω , temperature T and sediment concentration C . Since the dominant mode has the form of an inclined wave, the settling velocity of the sediment concentration field results in a horizontal phase shift between the T - and C -waves. This translates into a phase shift between the stabilizing and destabilizing vorticity waves associated with these two scalars, which in turn causes the instability.

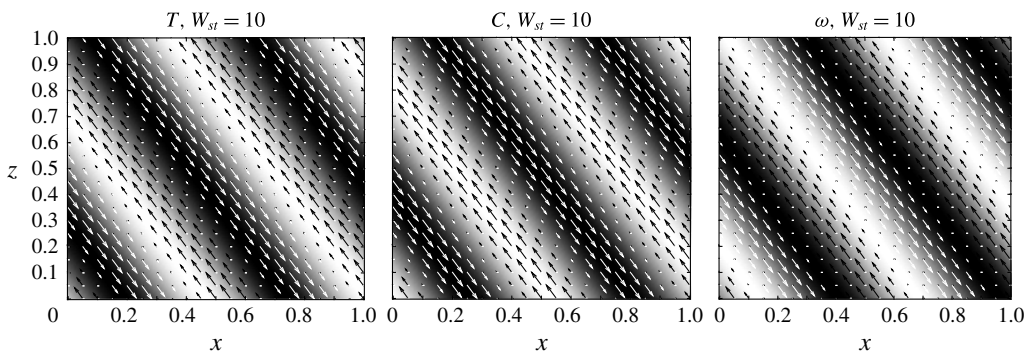


FIGURE 5. $Pr = 7$, $\tau = 1$, $R_\rho = 1.5$, $\phi = 0$, $W_{st} = 10$: two-dimensional dominant mode eigenfunctions of temperature T , sediment concentration C and vorticity ω , for the case of a purely settling-driven instability. Superimposed are the velocity vectors corresponding to the u - and w -eigenfunctions. The horizontal and vertical axes are normalized by the size of the region shown, which is 50. Note the slight phase shift between the C - and T -eigenfunctions, which is responsible for the instability.

4.2. Influence of double diffusion

We now proceed to systems with $\tau \neq 1$ and $W_{st} \neq 0$, in order to study the interaction of settling-driven and double-diffusive instabilities. In the following, our discussion will focus primarily on the effects of the settling velocity W_{st} under these conditions, with the remaining dimensionless parameters held fixed at $Pr = 7$, $\tau = 0.01$, $R_\rho = 1.5$ and $\phi = 0$, unless stated otherwise. Figure 6 shows the maximum value of the real part of the growth rate, λ_R , as function of the horizontal and vertical wavenumbers l and k , for three different values of the settling velocity W_{st} . Only unstable solutions $\lambda_R > 0$ are shown, and the mode with the largest growth rate $\lambda_{R,max}$ is again marked by an ‘ \times ’. Consistent with earlier results, e.g. Baines & Gill (1969), we find that for

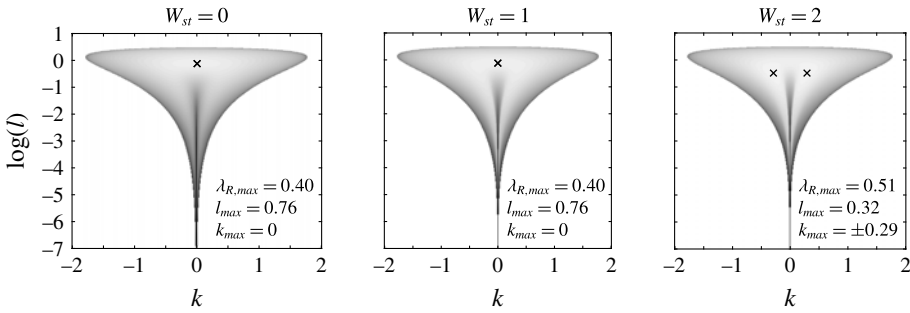


FIGURE 6. $Pr = 7$, $\tau = 0.01$, $R_\rho = 1.5$, $\phi = 0$: maximum real part λ_R of the growth rate as function of the vertical (k) and horizontal (l) wavenumbers, for three different values of the particle settling velocity W_{st} . Only positive values of λ_R are shown, and the mode with the largest growth rate $\lambda_{R,max}$ is marked with an ‘x’. The grey shading is scaled to $\log(\lambda_R)$. For $W_{st} = 0$, only the double-diffusive instability is active, and the most unstable mode is of elevator type. While the presence of a settling velocity does not modify the elevator mode, it destabilizes inclined waves. Beyond a critical value of W_{st} , the dominant mode takes the shape of inclined waves with $k \neq 0$.

the case of purely double-diffusive instability ($W_{st} = 0$) the most unstable mode has a vertical wavenumber $k = 0$. For moderate settling velocities, e.g. $W_{st} = 1$, fingering remains the dominant mode, and neither the most unstable horizontal wavenumber l_{max} nor the value of $\lambda_{R,max}$ vary as a function of W_{st} . This is consistent with our argument above that a settling velocity does not affect perturbations associated with the elevator mode.

Once the settling velocity exceeds a critical value of $W_{st,crit} \approx 1.05$, this picture changes, as the growth rates of modes with $k \neq 0$ overtake the elevator mode. For successively larger values of W_{st} , the most amplified horizontal wavenumber decreases, while its growth rate $\lambda_{R,max}$ increases. The above observation is confirmed by figure 7, which demonstrates that at the critical value of W_{st} the dominant instability mode switches from $k_{max} = 0$ to $k_{max} \neq 0$. For the present parameter combination, the horizontal and vertical wavenumbers of the dominant mode are similar in magnitude for W_{st} -values above approximately 1.5, so that its wavefronts are inclined at roughly 45° . The growth rate $\lambda_{R,max}$ of the dominant mode increases monotonically with W_{st} , while $\lambda_{I,max}$ decreases.

Figure 7(c) displays the ratio of the downward vertical velocity $-\lambda_{I,max}/k_{max}$ of the most unstable mode to the settling velocity W_{st} . We find that beyond the critical value of $W_{st,crit} \approx 1.05$ the downward velocity of the most unstable mode tends towards the particle settling velocity W_{st} , so that the ratio $-\lambda_{I,max}/(W_{st}k_{max})$ approaches unity.

4.3. Influence of the density ratio

Figure 8(a), which is similar to a corresponding figure in Reali *et al.* (2017) albeit for different parameters, analyses the influence of the density ratio on the heat–sediment system in the absence of lateral base state gradients. For vanishing settling velocity $W_{st} = 0$, we confirm the well-known result that only density ratios $R_\rho < 1/\tau$ are unstable. A positive settling velocity $W_{st} > 0$, on the other hand, immediately destabilizes all density ratios $R_\rho > 1/\tau$ as well. This destabilizing effect grows with the settling velocity. For a given value of $R_\rho < 1/\tau$, the growth rate is affected

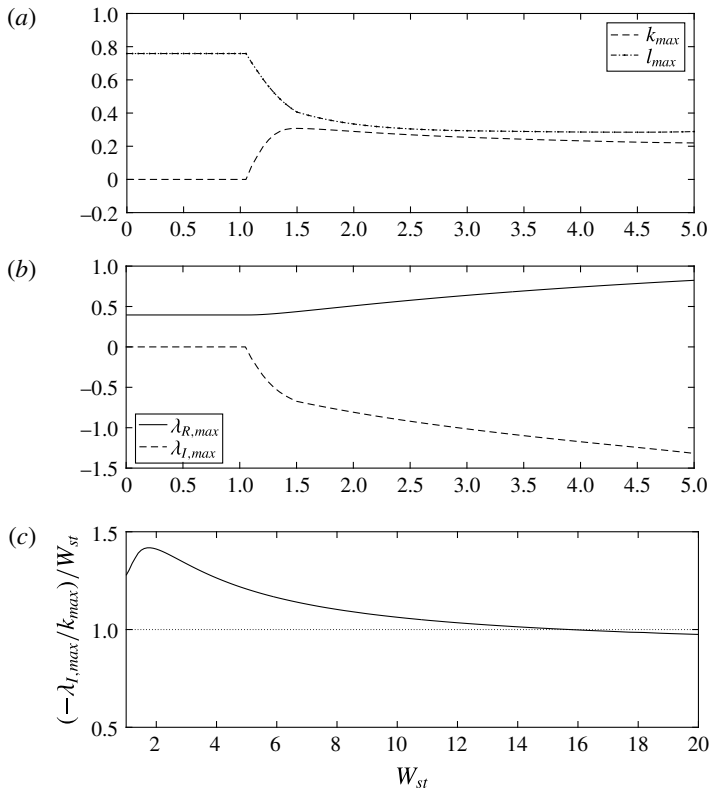


FIGURE 7. $Pr = 7$, $\tau = 0.01$, $R_\rho = 1.5$, $\phi = 0$: (a) most unstable horizontal (l_{max}) and vertical (k_{max}) wavenumbers as functions of the particle settling velocity W_{st} . Beyond the critical value of the settling velocity ($W_{st,crit} \approx 1.05$), settling-driven inclined waves overtake those of the double-diffusive elevator mode as the dominant instability mode. (b) Beyond $W_{st,crit}$, the growth rate $\lambda_{R,max}$ of the dominant mode increases uniformly with W_{st} , while the imaginary part of the growth rate $\lambda_{I,max}$ deviates from zero. (c) The ratio of the vertical phase velocity of the dominant mode $\lambda_{I,max}/k_{max}$ to the particle settling velocity. For large W_{st} this ratio approaches one, showing that the wave travels approximately with the particle settling velocity.

by the settling velocity only above a critical value of W_{st} , which is consistent with the results of § 4.2. This critical value of W_{st} decreases for larger density ratios. Within the regime where the growth rate is affected by the settling velocity, visual inspection indicates a power-law dependence of $\lambda_{R,max}$ on R_ρ

$$\lambda_{R,max} \propto R_\rho^{-n}, \quad (4.2)$$

where $n \approx 1$.

Figure 8(b–d) shows corresponding results for $\lambda_{I,max}$, l_{max} and k_{max} . For small values of W_{st} and $R_\rho < 1/\tau$, where the instability growth rate $\lambda_{R,max}$ is independent of the settling velocity, both $\lambda_{I,max}$ and k_{max} are identically zero, so that the dominant instability mode is elevator like and does not travel in the vertical direction. For larger W_{st} -values, on the other hand, inclined modes dominate across the entire R_ρ range. The intermediate value of $W_{st} = 1$ gives rise to three different regimes: near

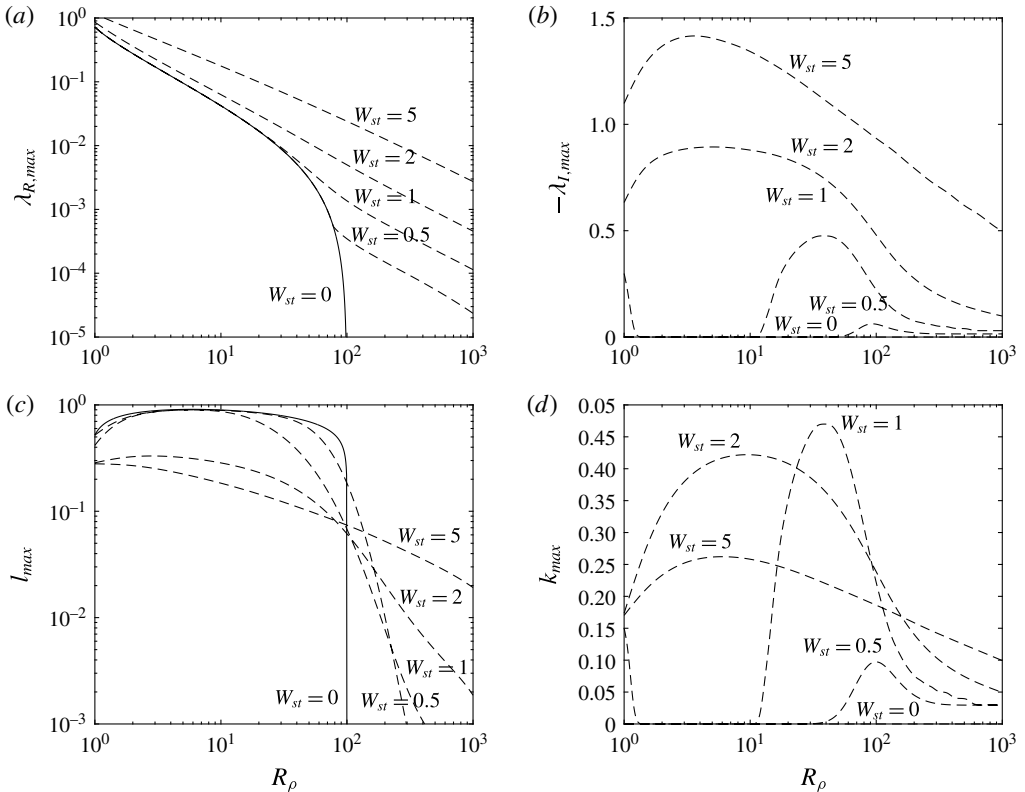


FIGURE 8. $Pr = 7$, $\tau = 0.01$, $\phi = 0$: variation of the dominant mode properties with the density ratio R_ρ and the settling velocity W_{st} , when both double-diffusive and settling-driven instabilities are present. (a) The maximum growth rate $\lambda_{R,max}$: for $W_{st} = 0$, only the double-diffusive instability is present, so that only density ratios $\tau < 1/R_\rho$ are unstable. For $W_{st} > 0$ the settling-driven mode destabilizes all density ratios. (b) The imaginary part $\lambda_{I,max}$ of the growth rate: for small values of W_{st} and $R_\rho < 1/\tau$, the dominant mode is of elevator type. (c) For large density ratios, the horizontal wavenumber l_{max} of the dominant mode decreases with R_ρ . (d) The vertical wavenumber k_{max} of the dominant mode peaks for intermediate density ratios.

$R_\rho \approx 1$ inclined waves are most amplified, for $1.14 \leq R_\rho \leq 10$ the elevator mode dominates and beyond that inclined modes are once again most unstable. Figure 8(c) demonstrates that for $R_\rho > 1/\tau$, larger values of W_{st} tend to favour shorter horizontal wavelengths.

4.4. Influence of the diffusivity ratio

An interesting picture emerges when we analyse the influence of the diffusivity ratio on the stability of the system for $Pr = 7$, $R_\rho = 1.5$, $\phi = 0$ and various values of the settling velocity W_{st} , cf. figure 9. In the absence of settling, the regime $\tau < 1/R_\rho$ is unstable to traditional double-diffusive fingering, with $\lambda_{I,max} = 0$. For $\tau \geq 5$, we observe the well-known oscillatory ‘diffusive’ instability regime with $\lambda_{I,max} > 0$. Without settling, the range in between these two τ -values is stable, with $\lambda_{I,max} < 0$. In the presence of settling, this intermediate τ -range becomes unstable to inclined

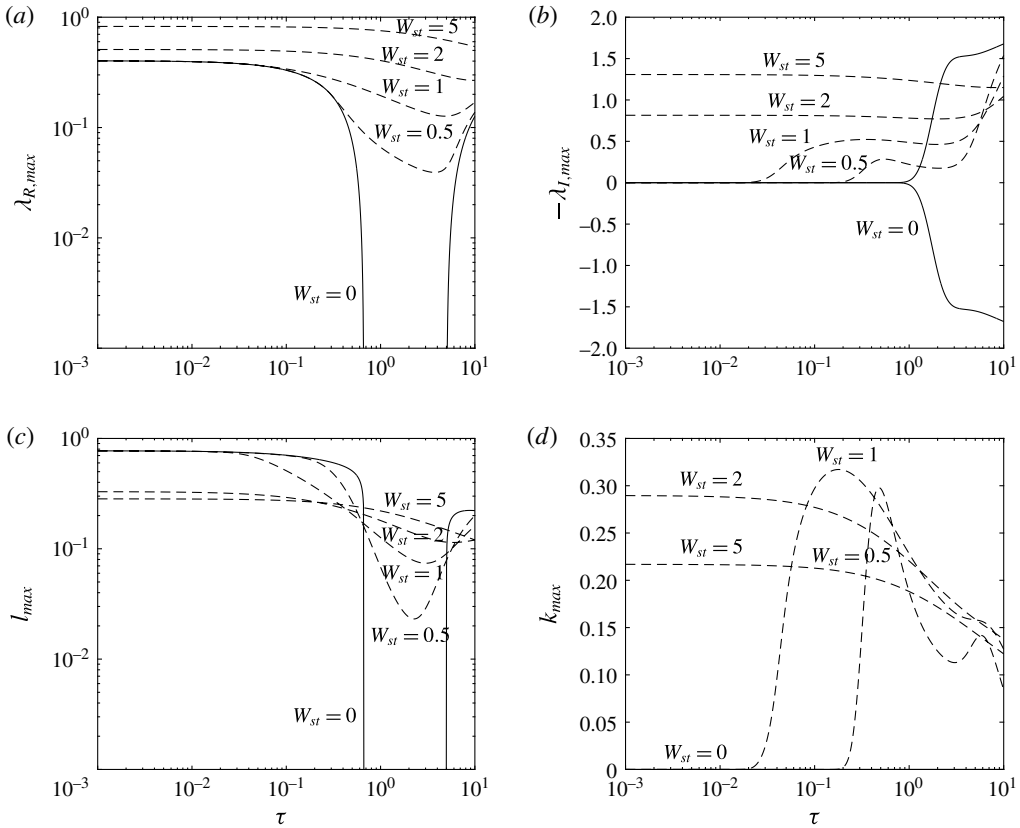


FIGURE 9. $Pr = 7$, $R_\rho = 1.5$, $\phi = 0$: variation of the dominant mode properties with the diffusivity ratio τ and the settling velocity W_{st} . For $W_{st} = 0$, double-diffusive fingering exists below $\tau < 1/R_\rho$, and oscillatory double diffusion with $\lambda_{I,max} > 0$ is seen for $\tau \geq 1$. For $W_{st} > 0$ the intermediate τ -range becomes destabilized as well, with regard to downward travelling, inclined waves. Consequently, in the presence of settling the flow is unstable for all values of τ .

waves, with larger settling velocities resulting in higher growth rates. Hence in the presence of settling the flow is unstable for all τ -values. This indicates that the system develops instabilities even if the unstably stratified ‘sediment’ component diffuses more rapidly than the stably stratified ‘temperature’ component, which may occur for certain sediment grain sizes (Reali *et al.* 2017). Figure 9 furthermore indicates that for the traditional fingering regime $\tau < 1/R_\rho$ the critical value of W_{st} depends on τ .

4.5. Influence of lateral gradients

Lateral gradients break the overall symmetry of the system with regard to $k = 0$, as shown in figure 10(a). As we introduce a lateral gradient of $\phi = 0.1$, the dominant mode in the absence of settling switches from $k = 0$ to $k < 0$. Figure 10(b) shows the inclined temperature base state, which is density compensated by a corresponding sediment concentration field, so that all base state density contours are horizontal. Figure 10(c) displays the vorticity eigenfunction for the most unstable mode with

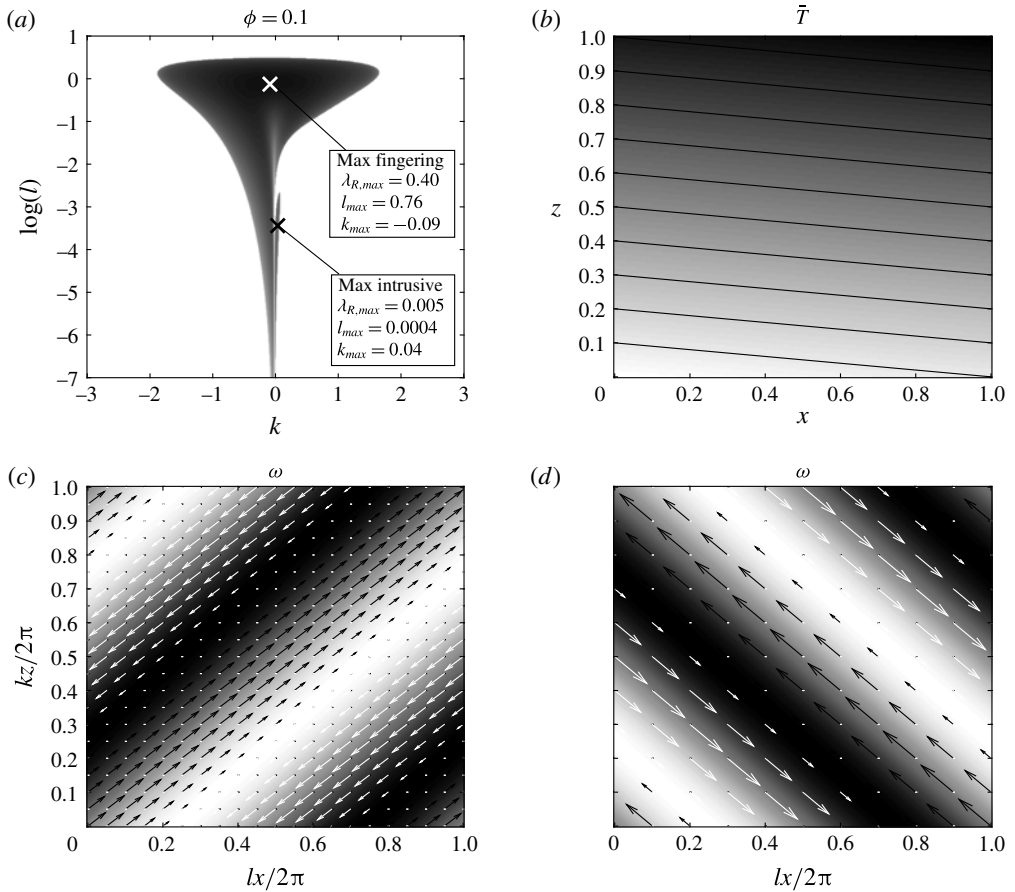


FIGURE 10. $Pr=7$, $\tau=0.01$, $R_\rho=1.5$, $\phi=0.1$, $W_{st}=0$: (a) maximum real part λ_R of the growth rate as function of the vertical (k) and horizontal (l) wavenumbers: a lateral base state gradient breaks the symmetry, by shifting the dominant double-diffusive fingering mode to $k_{max} < 0$. At the same time, a new intrusive instability mode appears for small k and l . (b) Contours of the base state temperature field. (c) The vorticity eigenfunction for the dominant fingering mode with $l=0.76$ and $k=-0.09$. (d) The vorticity eigenfunction for the intrusive mode. Note that the wavefronts for the fingering and intrusive modes are inclined in opposite directions.

$l = 0.76$ and $k = -0.09$. We find that its wavefronts are tilted in the opposite direction from the base state temperature and sediment concentration contours. At the same time, a new instability mode in the shape of a small ‘leaf’ appears for $k > 0$ and large horizontal wavelengths in the lower right quadrant of figure 10(a). This unstable region represents the intrusive mode discussed by Medrano *et al.* (2014). Its perturbation wavefronts are tilted in the same direction as the base state temperature and sediment concentration contours, as can be seen in figure 10(d).

By generating plots similar to figure 10(a), but for different values of W_{st} , we can analyse how these two distinct instability modes are affected by settling. We find that the growth rate of the dominant fingering modes increases with the settling velocity, and its horizontal wavelength increases. The intrusion mode initially becomes more

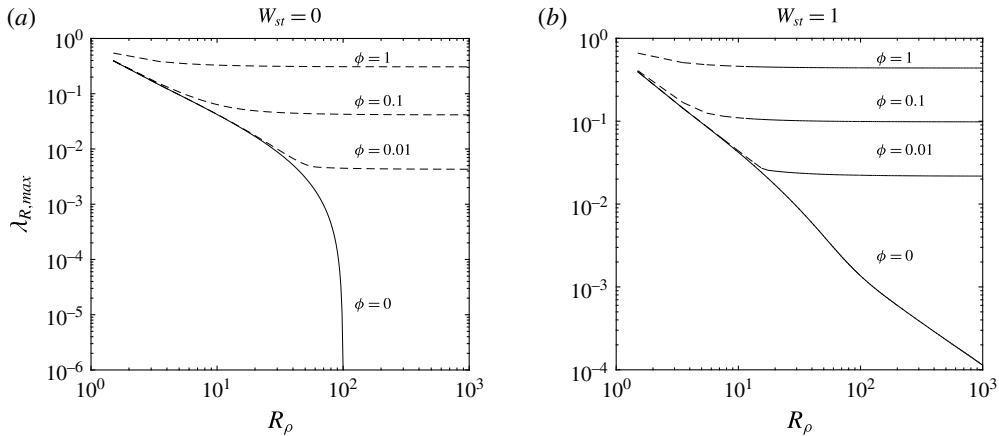


FIGURE 11. $Pr = 7$, $\tau = 0.01$: variation of the growth rate $\lambda_{R,max}$ of the dominant mode with the density ratio R_ρ and the lateral base state gradient ϕ , for two different values of W_{st} . A lateral base state gradient $\phi > 0$ destabilizes the flow for all density ratios R_ρ . A settling velocity $W_{st} > 0$ also destabilizes $\phi = 0$.

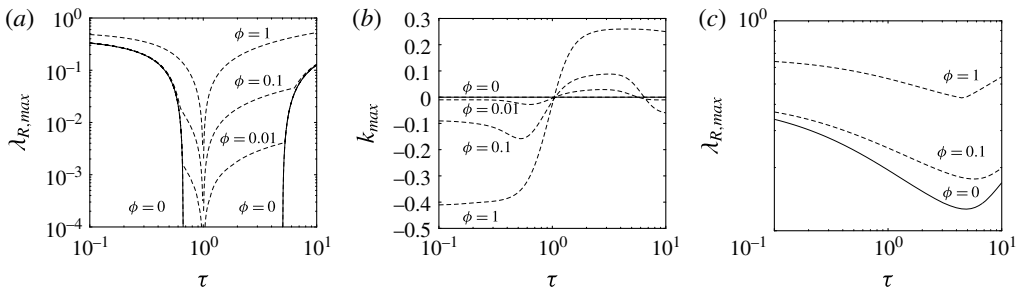


FIGURE 12. $Pr = 7$, $R_\rho = 1.5$: variation of (a) the growth rate $\lambda_{R,max}$, and (b) the vertical wavenumber k_{max} of the dominant mode with the diffusivity ratio τ and the lateral base state gradient ϕ , for $W_{st} = 0$. Lateral base state gradients destabilize all diffusivity ratios $\tau \neq 1$. For $\tau > 1$, the dominant waves are inclined in the opposite direction as compared to $\tau < 1$. (c) For $W_{st} = 1$ all diffusivity ratios are unstable, including $\tau = 1$.

prominent as W_{st} increases, but beyond $W_{st} \approx 1$ the shape of its lobe varies only weakly with W_{st} .

Figure 11(a) confirms the earlier observation by Holyer (1983) that, in the absence of a settling velocity, lateral base state gradients destabilize the flow for all density ratios R_ρ . In the regime $R_\rho < 1/\tau$, which is unstable even in the absence of lateral base state gradients, the influence of ϕ on the growth rate is felt only above a critical value of ϕ , which depends on R_ρ . In the presence of a settling velocity W_{st} , we find that all values of ϕ are destabilized for all density ratios, including $\phi = 0$, cf. figure 11(b).

Interesting dynamics is observed when we plot the growth rate as a function of the diffusivity ratio τ , for select lateral gradient values ϕ and in the absence of a settling velocity, cf. figure 12. Consistent with earlier findings by other authors, for $\tau < 1/R_\rho$ all values of $\phi \geq 0$ are unstable. For $\phi > 0$ (but not for $\phi = 0$), the interval $1/R_\rho < \tau < 1$ becomes destabilized as well. For $\tau = 1$, all values of ϕ are stable, since neither the double-diffusive nor the settling-driven instability are active. However, for $\tau > 1$,

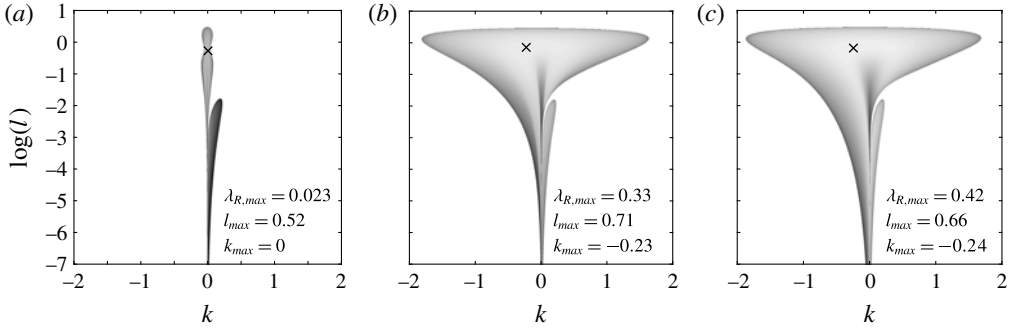


FIGURE 13. $\tau = 0.01$, $R_\rho = 1.5$, $\phi = 0.1$, $W_{st} = 1$: maximum real part λ_R of the dominant mode growth rate as function of the vertical (k) and horizontal (l) wavenumbers, for $Pr = 10^{-3}$ (a), $Pr = 1$ (b), and $Pr = 10^3$ (c). The dominant mode is marked with ‘x’. The intrusion mode shows little dependence on Pr , while the dominant fingering mode is largely independent of Pr for $Pr \geq 1$.

all lateral gradients $\phi > 0$ are destabilized once again, and for $\tau > 5$ we observe the oscillatory ‘diffusive’ mode described earlier for all $\phi \geq 0$. Also note that k changes its sign as τ goes from < 1 to > 1 , indicating that the wavefronts are inclined in opposite directions in these two regimes. Figure 12(c) analyses the influence of lateral gradients on the overall properties of the instability as a function of τ , in the presence of a settling velocity W_{st} . Now all values of τ , including $\tau = 1$, are destabilized.

In the context of certain astrophysical applications a suitably defined Prandtl number can become very small (Medrano *et al.* 2014), so that it is of interest to examine how the dominant instability mode varies with Pr . Figure 13 indicates that the scenarios for $Pr = 1$ and $Pr = 10^3$ are quite similar with regard to the maximum growth rate, the dominant horizontal and vertical wavenumbers, and the presence of the intrusive mode. For $Pr = 10^{-3}$ we find that the traditional fingering mode has become less prominent, while the intrusive mode remains relatively unaffected by Pr . This suggests that in astrophysical applications the intrusion mode should become increasingly more important as compared to the fingering mode (Medrano *et al.* 2014).

5. Direct numerical simulation results

In order to analyse the nonlinear evolution of the various instabilities discussed above, we present results from a series of two-dimensional DNS. We solve the governing dimensionless equations by means of a hybrid pseudospectral/compact finite-difference spatial scheme combined with the low-storage Runge–Kutta/Crank–Nicolson time stepping method of Williamson (1980). The pseudospectral method is used in the horizontal direction, while the vertical direction is discretized using a compact finite-difference method (Lele 1992) of up to eighth order. The simulations employ periodic boundary conditions for the perturbation fields in both directions. For a more detailed description of the code and its validation, we refer the reader to Burns & Meiburg (2015). We have also compared DNS growth rates for small perturbations with linear stability results, and we generally found agreement to within a fraction of one per cent. All simulations are initiated with random white noise perturbations to the temperature and sediment concentration fields. Movies of all of the DNS to be discussed below are available in the online supplemental material at <https://doi.org/10.1017/jfm.2017.94>.

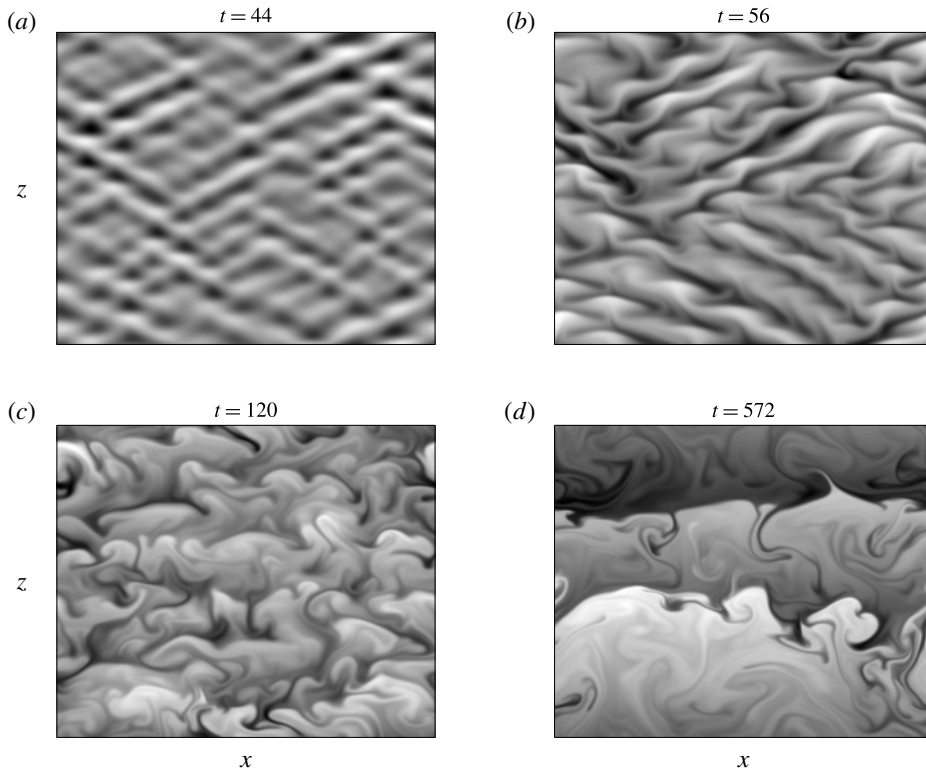


FIGURE 14. Snapshots of the sediment concentration perturbation field from a two-dimensional simulation for $Pr = 7$, $\tau = 1$, $R_\rho = 1.5$, $\phi = 0$ and $W_{st} = 1$, with white noise as the initial condition. The domain of size $L_x = L_z = 256$ is discretized by $N_x = N_z = 1024$ grid points. The instability is purely settling driven, and the wavelengths of the emerging dominant inclined modes are consistent with linear stability results. Eventually, these inclined waves give way to horizontal layers. The time-dependent evolution of the sediment concentration perturbation field in a downward moving reference frame is shown by movie 1 in the supplemental material.

Figure 14 presents DNS results for the sediment concentration perturbation field, for the parameter combination of $Pr = 7$, $\tau = 1$, $R_\rho = 1.5$, $\phi = 0$ and $W_{st} = 1$. Both species have identical diffusivities, so that double-diffusive effects are absent for this flow, and the instability is driven exclusively by settling. The linear stability results of figure 2 predict dominant instability modes for this case in the form of inclined waves with $l_{max} = 0.12$ and $k_{max} = \pm 0.23$, corresponding to most amplified horizontal and vertical wavelengths near 52 and 27, respectively. These values are consistent with the DNS observation in figure 14(a) of approximately ten inclined wavefronts over the vertical domain length of $L_z = 256$, and five to six wavefronts over the horizontal domain length of $L_x = 256$. Figure 14(b) demonstrates that as a result of the random nature of the initial perturbations, some parts of the flow field become dominated by wavefronts inclined to the right, and other regions by wavefronts inclined to the left. Figure 14(c,d) shows that these inclined wavefronts eventually give way to horizontal layers. The secondary instabilities responsible for the growth of these horizontal layers are analysed in detail in the companion paper by Reali *et al.* (2017).

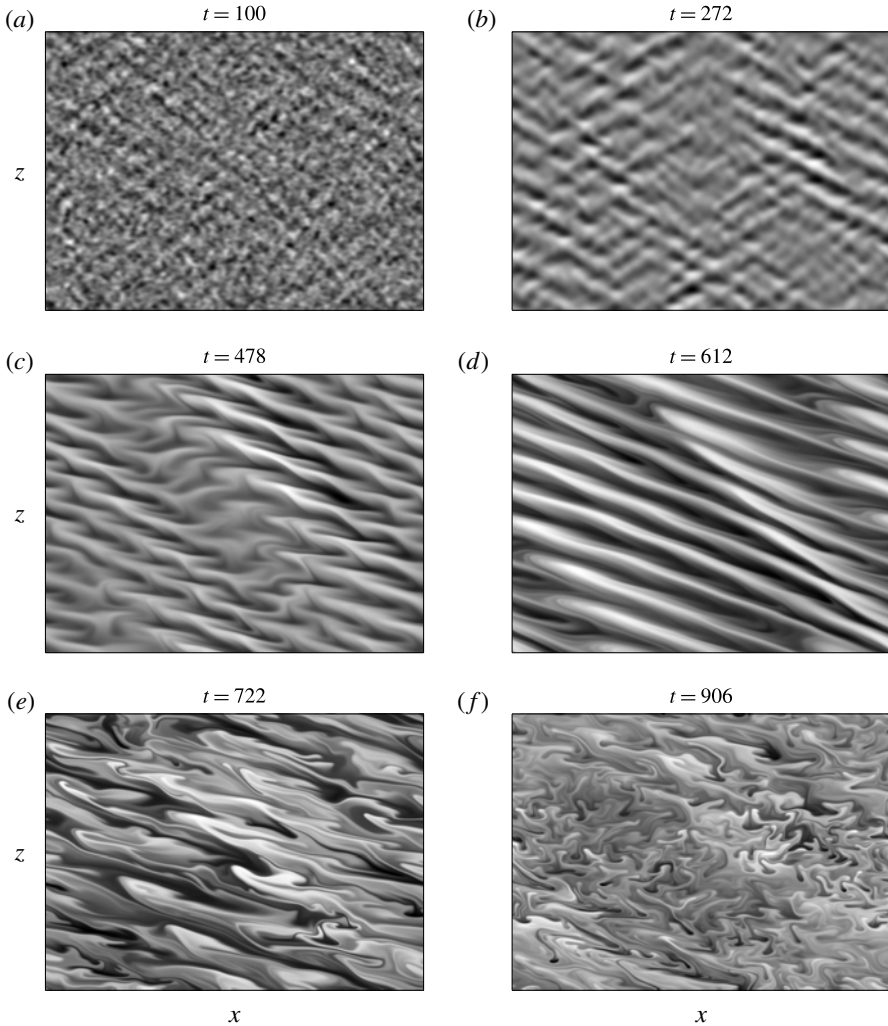


FIGURE 15. Snapshots of the sediment concentration perturbation field from a two-dimensional simulation for $Pr = 7$, $\tau = 0.01$, $R_\rho = 150$, $\phi = 0$ and $W_{st} = 5$, initiated by white noise. The domain of size $L_x = L_z = 256$ is discretized by $N_x = 1024$ and $N_z = 4096$ grid points. Since $R_\rho > 1/\tau$, double-diffusive instabilities would not be amplified for $W_{st} = 0$. Inclined waves emerge that dominate the flow during the early stages. Eventually, these inclined waves develop secondary instabilities that cause the flow to break down into small-scale structures. The time-dependent evolution of the sediment concentration perturbation field in a downward moving reference frame is shown by movie 2 in the supplemental material.

Figure 15 displays the nonlinear evolution of the sediment concentration perturbation field for parameter values $Pr = 7$, $\tau = 0.01$, $R_\rho = 150$, $\phi = 0$ and $W_{st} = 5$. While the diffusivities of the two scalar fields differ by a factor of 100, $R_\rho > 1/\tau$, so that double-diffusive instabilities would not be amplified in the absence of settling, see the linear stability results in figure 8. For $W_{st} = 5$, on the other hand, the linear analysis predicts a growing instability in the form of inclined waves with $l_{max} = 0.07$ and

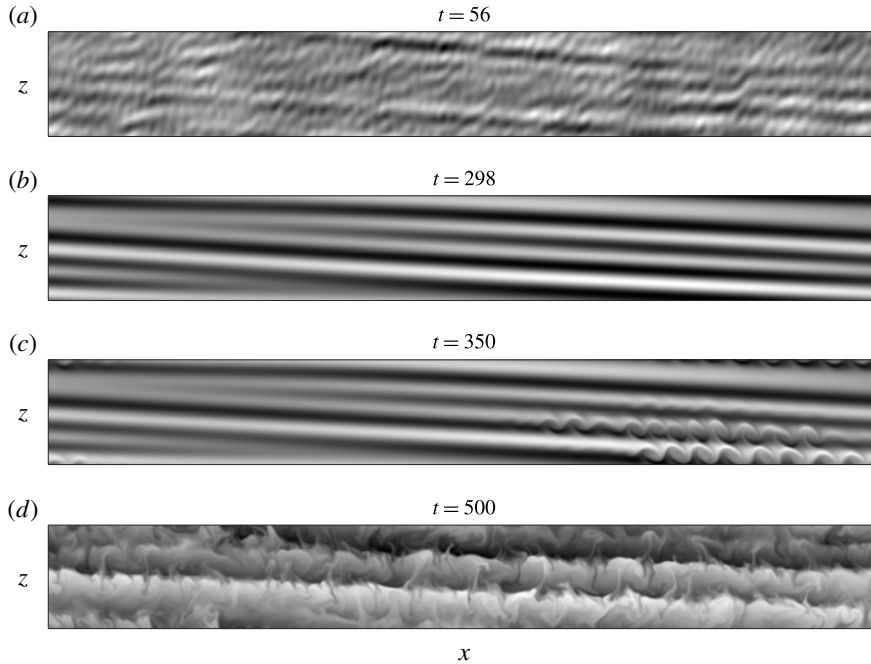


FIGURE 16. Snapshots of the sediment concentration perturbation field from a two-dimensional simulation for $Pr = 7$, $\tau = 5$, $R_\rho = 1.5$, $\phi = 0.1$ and $W_{st} = 0$, initiated by white noise. The domain of size $L_x = 2560$ and $L_z = 256$ is discretized by $N_x = 4096$ and $N_z = 1024$ grid points. The flow is initially dominated by an intrusive instability mode. At later times, shear-driven instabilities grow along the interfaces separating neighbouring intrusions, which eventually give rise to small-scale structures superimposed on the intrusion-dominated flow. The time-dependent evolution of the sediment concentration perturbation field can be viewed in movie 3 in the supplemental material.

$k_{max} = \pm 0.18$, corresponding to horizontal and vertical wavelengths of approximately 90 and 35, respectively. Again, these values are consistent with the dominant modes observed in the DNS shown in figure 15(a–d). While panels (a) and (b) indicate the emergence of waves inclined in both directions, panels (c) and (d) show that one family of inclined waves eventually dominates of the flow field. Panels (e) and (f) demonstrate that these waves develop secondary instabilities and eventually break down into small-scale structures. By the final time of the simulation, dominant horizontal layers have not evolved.

Figure 16 shows results for a DNS with a horizontal base state gradient, so that it is dominated by intrusive instabilities, but without Stokes settling, for $Pr = 7$, $\tau = 5$, $R_\rho = 1.5$, $\phi = 0.1$ and $W_{st} = 0$. Note that here the unstably stratified, sedimenting scalar diffuses more rapidly. The linear stability results of figure 12 predict dominant waves inclined to the lower right with $l_{max} = 0.003$ and $k_{max} = 0.09$, corresponding to horizontal and vertical wavelengths of approximately 2000 and 70, respectively. Once again, the linear stability predictions are borne out by the early DNS results of panels (a) and (b). Panel (c) shows the development of shear-driven instabilities along the interfaces separating neighbouring intrusions, while panel (d) indicates the emergence of energetic small-scale structures superimposed on the primarily horizontal intrusions.

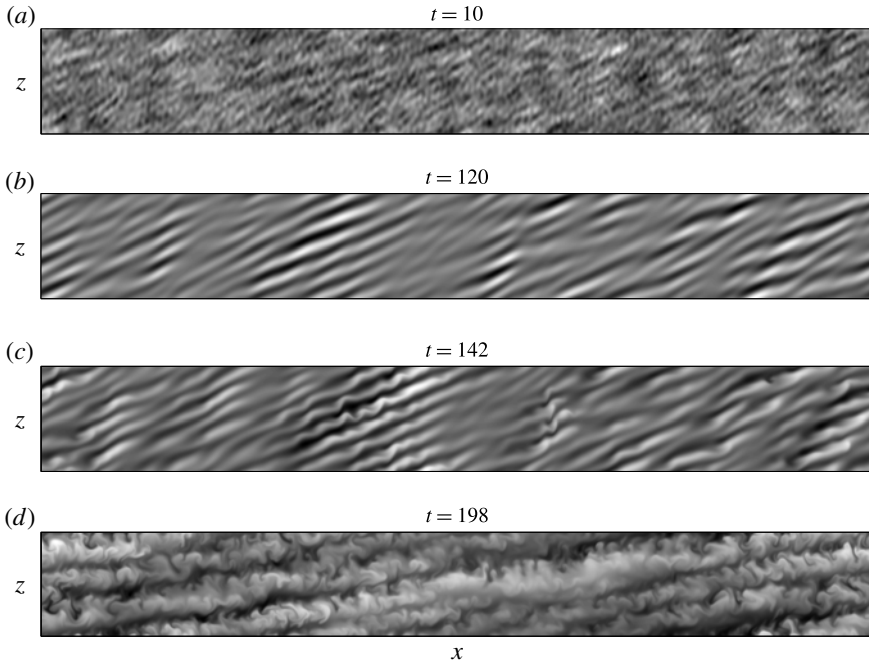


FIGURE 17. Snapshots of the sediment concentration perturbation field from a two-dimensional simulation for $Pr = 7$, $\tau = 5$, $R_\rho = 1.5$, $\phi = 0.1$ and $W_{st} = 0.5$, initiated by white noise. The domain of size $L_x = 2560$ and $L_z = 256$ is discretized by $N_x = 4096$ and $N_z = 1024$ grid points. The time-dependent evolution of the sediment concentration perturbation field can be viewed in movie 4 in the supplemental material.

The case shown in figure 17 is identical to that of figure 16, except that it has a settling velocity of 0.5. The linear stability results now predict dominant waves inclined to the lower left with $l_{max} = 0.03$ and $k_{max} = -0.13$, corresponding to horizontal and vertical wavelengths of approximately 200 and 50, which is consistent with the early DNS results of panels (a) and (b). The comparison of figures 16 and 17 demonstrates that even for flows with horizontal base state gradients, settling can strongly alter the linear and nonlinear flow evolution.

6. Summary

We have presented a linear stability analysis of overall stably stratified fluids whose density depends on two components, where one of these components is unstably stratified and settles. We focus on constant-gradient base states in unbounded domains. The analysis demonstrates that settling generates a phase shift between the perturbation fields of the two scalar components, which gives rise to a novel instability mode driven by settling. This instability mechanism favours the growth of inclined waves, and is active for all density and diffusivity ratios, including for cases in which the two scalars diffuse at identical rates. If the scalar components have unequal diffusivities, the settling-driven instability mode competes with the elevator mode of the classical fingering instability. Detailed linear stability results clarify the balance between the settling-driven and double-diffusive instability modes as a function of the governing dimensionless parameters, and DNS results illustrate the nonlinear

competition between the settling mode, the double-diffusive fingering mode and the intrusive mode.

In order to discuss applications of our findings to various geophysical situations, we need to know the expected non-dimensional values of W_{st} and τ for various sediment sizes. These have been computed by Reali *et al.* (2017). They found that for silicate-based particles (clays, silts and sand for instance) of radius r , settling in ambient water at room temperature (where $d \simeq 0.01$ m, see Radko 2013), $W_{st} \simeq 0.45(r/10 \mu\text{m})^2$ in the Stokes regime. Hence, micron-sized clay particles have W_{st} of order 10^{-2} while fine sand ($r \simeq 0.1$ mm) has $W_{st} \simeq 10^2$. Assuming that the major contribution to the particle diffusivity comes from hydrodynamic diffusion (Segre *et al.* 2001), they also found that $\tau \simeq rW_{st}/d$, implying that $\tau \simeq 10^{-4}$ for $10 \mu\text{m}$ size particles, increasing rapidly to $\tau \simeq 0.1$ for 0.1 mm-sized particles. The fiducial parameter values we have used in this paper ($\tau = 0.01$ and W_{st} ranging from 0.5 to 10) would therefore be appropriate for particles a few tens of microns in size (e.g. very fine sand). The above linear stability results indicate that at these W_{st} -values the settling instability mode may well dominate over the traditional double-diffusive fingering mode.

To be more precise, let us estimate approximate dimensional length and time scales of the settling-driven instability. Using characteristic length and time scales of $d \sim 0.01$ m, and $t \sim 10^3$ s appropriate for water at ambient temperature, and assuming a moderate value of the density ratio (i.e. not too large) we find that a typical dimensionless wavenumber in the range of 0.1 (e.g. figures 8 and 9) translates into a dimensional instability wavelength of the order of 60 cm. Meanwhile, a dimensionless growth rate of the order of 0.1 to 1 corresponds to a dimensional growth time scale of the order of 10^3 s– 10^4 s, i.e. on the order of an hour. These ballpark estimates consequently suggest that the settling-driven instability reported here may be relevant in oceans and lakes.

R_ρ -values in river outflows can range from near unity for extremely high sediment loading to very large values $R_\rho \gg 1$ for cases with light sediment loading. The above results imply that even for conditions of $R_\rho > 1/\tau$, where traditional double-diffusive fingering is suppressed, instabilities can evolve as a result of settling.

We hope that the linear stability analysis presented here will serve as the starting point for clarifying several additional features of two-component stratified flows with settling. It will be particularly interesting to quantify the conditions for layer formation, which was observed both here and in the simulations of Reali *et al.* (2017). While the three-dimensional simulations of Reali *et al.* (2017) were limited to $Pr = 7$ and $\tau = 0.3$, it would be desirable to obtain DNS data for smaller diffusivity ratios such as $\tau = 0.01$, along with the related transport rates, to shed additional light on the layer formation issue.

Acknowledgements

The authors gratefully acknowledge Professors B. Bamieh and M. Wells for helpful discussions, and N. Konopliv for the use of his nonlinear simulation code. Financial support was provided by the Saudi Arabian Oil Company (Saudi Aramco) to A.A., and by NSF grants CBET-1438052 to E.M. and CBET-1437275 to P.G., as well as by grant DN NSWC N00174-16-C-0013 to E.M. Computational resources for this work were made available by the Extreme Science and Engineering Discovery Environment (XSEDE), which is supported by NSF grant TGCTS150053.

Supplementary movies

Supplementary movies are available at <https://doi.org/10.1017/jfm.2017.94>.

REFERENCES

- ALLDREDGE, A. & COHEN, Y. 1987 Can microscale chemical patches persist in the sea? Microelectrode study of marine snow, fecal pellets. *Science* **235** (4789), 689–691.
- BAINES, P. G. & GILL, A. E. 1969 On thermohaline convection with linear gradients. *J. Fluid Mech.* **37**, 289–306.
- BURNS, P. & MEIBURG, E. 2012 Sediment-laden fresh water above salt water: linear stability analysis. *J. Fluid Mech.* **691**, 279–314.
- BURNS, P. & MEIBURG, E. 2015 Sediment-laden fresh water above salt water: nonlinear simulations. *J. Fluid Mech.* **762**, 156–195.
- CARAZZO, G. & JELLINEK, A. M. 2013 Particle sedimentation and diffusive convection in volcanic ash-clouds. *J. Geophys. Res.* **118** (4), 1420–1437.
- CAREY, S. 1997 Influence of convective sedimentation on the formation of widespread tephra fall layers in the deep sea. *Geology* **25** (9), 839–842.
- CHEN, C. F. 1997 Particle flux through sediment fingers. *Deep-Sea Res. I* **44** (9), 1645–1654.
- DAVARPANAH, J. S. & WELLS, M. G. 2016 Enhanced sedimentation beneath particle-laden flows in lakes and the ocean due to double-diffusive convection. *Geophys. Res. Lett.* **43** (20), 10883–10890.
- GREEN, T. 1987 The importance of double diffusion to the settling of suspended material. *Sedimentology* **34** (2), 319–331.
- GREEN, T. & DIEZ, T. 1995 Vertical plankton transport due to self-induced convection. *J. Plankton Res.* **17** (9), 1723–1730.
- HOLYER, J. Y. 1983 Double-diffusive interleaving due to horizontal gradients. *J. Fluid Mech.* **137**, 347–362.
- HOYAL, D., BURSIK, M. & ATKINSON, J. 1999a The influence of diffusive convection on sedimentation from buoyant plumes. *Mar. Geol.* **159** (1), 205–220.
- HOYAL, D., BURSIK, M. & ATKINSON, J. 1999b Settling-driven convection: a mechanism of sedimentation from stratified fluids. *J. Geophys. Res.* **104** (C4), 7953–7966.
- LAMPITT, R., ACHTERBERG, E., ANDERSON, T., HUGHES, J. A., IGLESIAS-RODRIGUEZ, M. D., KELLY-GERREYN, B. A., LUCAS, M., POPOVA, E. E., SANDERS, R., SHEPHERD, J. G. *et al.* 2008 Ocean fertilization: a potential means of geoengineering? *Phil. Trans. R. Soc. Lond. A* **366** (1882), 3919–3945.
- LELE, S. K. 1992 Compact finite difference schemes with spectral-like resolution. *J. Comput. Phys.* **103** (1), 16–42.
- MANVILLE, V. & WILSON, C. J. N. 2004 Vertical density currents: a review of their potential role in the deposition and interpretation of deep-sea ash layers. *J. Geol. Soc.* **161** (6), 947–958.
- MANZELLA, I., BONADONNA, C., PHILLIPS, J. C. & MONNARD, H. 2015 The role of gravitational instabilities in deposition of volcanic ash. *Geology* **43** (3), 211–214.
- MAXWORTHY, T. 1999 The dynamics of sedimenting surface gravity currents. *J. Fluid Mech.* **392**, 27–44.
- MEDRANO, M., GARAUD, P. & STELLMACH, S. 2014 Double-diffusive mixing in stellar interiors in the presence of horizontal gradients. *Astrophys. J. Lett.* **792** (2), L30.
- PARSONS, J., BUSH, J. & SYVITSKI, J. 2001 Hyperpycnal plume formation from riverine outflows with small sediment concentrations. *Sedimentology* **48** (2), 465–478.
- PARSONS, J. & GARCÍA, M. 2000 Enhanced sediment scavenging due to double-diffusive convection. *Intl J. Sedim. Res.* **70** (1), 47–52.
- RADKO, T. 2013 *Double-diffusive Convection*. Cambridge University Press.
- REALI, J. F., GARAUD, P., ALSINAN, A. & MEIBURG, E. 2017 Layer formation in sedimentary fingering convection. *J. Fluid Mech.* **816**, 268–305.

- ROUHNIA, M. & STROM, K. 2015 Sedimentation from flocculated suspensions in the presence of settling-driven gravitational interface instabilities. *J. Geophys. Res.* **120** (9), 6384–6404.
- RUDDICK, B. R. & TURNER, J. S. 1979 The vertical length scale of double-diffusive intrusions. *Deep-Sea Res. A* **26** (8), 903–913.
- SÁNCHEZ, X. & ROGET, E. 2007 Microstructure measurements and heat flux calculations of a triple-diffusive process in a lake within the diffusive layer convection regime. *J. Geophys. Res.* **112** (C2), C02012.
- SCHEU, K. R., FONG, D. A., MONISMITH, S. G. & FRINGER, O. B. 2015 Sediment transport dynamics near a river inflow in a large alpine lake. *Limnol. Oceanogr.* **60** (4), 1195–1211.
- SCHULTE, B., KONOPLIV, N. & MEIBURG, E. 2016 Clear salt water above sediment-laden fresh water: Interfacial instabilities. *Phys. Rev. Fluids* **1** (1), 012301.
- SEGRE, P. N., LIU, F., UMBANHOWAR, P. & WEITZ, D. A. 2001 An effective gravitational temperature for sedimentation. *Nature (London)* **409**, 594.
- STERN, M. E. 1960 The salt-fountain and thermohaline convection. *Tellus* **12** (2), 172–175.
- STERN, M. E. 1967 Lateral mixing of water masses. In *Deep Sea Research and Oceanographic Abstracts*, vol. 14, pp. 747–753. Elsevier.
- TURNER, J. S. 1979 *Buoyancy Effects in Fluids*. Cambridge University Press.
- TURNER, J. S. 1985 Multicomponent convection. *Annu. Rev. Fluid Mech.* **17** (1), 11–44.
- WILLIAMSON, J. H. 1980 Low-storage Runge–Kutta schemes. *J. Comput. Phys.* **35** (1), 48–56.
- YU, X., HSU, T. & BALACHANDAR, S. 2013 Convective instability in sedimentation: linear stability analysis. *J. Geophys. Res.* **118** (1), 256–272.
- YU, X., HSU, T. & BALACHANDAR, S. 2014 Convective instability in sedimentation: 3-d numerical study. *J. Geophys. Res.* **119** (11), 8141–8161.